X-ray Characterization and Spray Measurements of ECN Spray G Using Alternative Fuels at Flashing Conditions

Brandon A. Sforzo*, Aniket Tekawade, Katarzyna E. Matusik, Alan L. Kastengren, Jan Ilavsky, Christopher F. Powell
Argonne National Laboratory, 9700 S. Cass Ave, Lemont, IL 60439, USA
*Corresponding author: bsforzo@anl.gov

Abstract
Detailed spray measurements for the Engine Combustion Network "Spray G" have been collected while operating at flashing conditions. Time-resolved fuel density was measured through tomographic x-ray radiography for neat iso-octane and a blend of 80% iso-octane with either 20% butanol or 20% ethanol by volume under a flash-boiling condition. Lastly, these same fuels were used during the collection of ultra small angle X-ray scattering (USAXS) measurements to quantify the specific surface area of the spray in the near-nozzle region. Spray density profiles generated through tomographic reconstruction of the radiography measurements reveal the high dispersion of the fuel under the flashing condition. This injection behavior also causes the individual plumes to collapse and interact with each other, which can lead to additional flow field perturbations. These maps also show density discrepancies between the fuel blends caused by their differing vaporization profiles. The spray differences between these fuels are further highlighted through the specific surface area profiles of droplets in the plumes. This combination of radiography and USAXS measurements provide a valuable quantification of the resulting spray morphology.

Keywords
X-ray, Radiography, USAXS, Fuels, ECN, Spray G

Introduction

Social and environmental concerns continually encourage improvements toward combustion efficiency and reduced emissions. For light-duty and passenger automobiles, Gasoline Direct Injection(GDI) systems offer many theoretical benefits over older gasoline technologies, like port-fuel injection, including improved efficiency and reduction in CO_2 output [1]. As a result, GDI has been implemented by many manufacturers, but with unanticipated drawbacks. For instance, particulate matter (PM) emissions are greater than expected [2] due to issues associated with poor mixing and wall wetting [3], and measurable unburned hydrocarbons and CO are the result of incomplete combustion.
One approach to overcome these emissions issues has been the adoption of bio-alcohol fuel blends [4]. Components such as ethanol, and second generation fuels such as butanol [5], also have the added benefits of being a renewable resource and reduce dependency on fossil fuels [6].
For these GDI conditions, it is common that the fuel introduction occurs at elevated temperatures and partial vacuum for many control schemes. With many gasoline distillates and the alcohols of interest, this can amount to a flash-boiling condition. In practice, flash boiling occurs when the liquid is delivered at high pressure to the hot injector and then undergoes a rapid decompression, leaving it in a metastable, superheated state [7].
These particular conditions, as applied to the injection process for GDI systems, has resulted in morphological changes to the fuel atomization and mass distribution. Considerable work has experimentally characterized the plume behavior for multi-hole injectors and single-component fuels, where, upon transitioning through a flash-boiling condition, the individual plumes interacted with each other and collapsed [8, 9]. This plume interaction and subsequent spray collapse have a significant effect on the fuel distribution at the beginning and end of injection [10], and therefore, physical models have been developed to relate the plume spreading and collapse behavior to the injector, injection, and fuel properties [11]. These recent studies have centered on conditions and geometries defined by the Engine Combustion Network (ECN) [12], which serves as a hub for experimental and modeling findings for internal combustion engine research. Following the experimental findings, high-fidelity computational fluid dynamics models have been examined under flashing and non-flashing conditions to reveal similar plume behavior and unique internal flow phenomena, which call for additional investigations into the internal and near-nozzle flow physics [13].
This work will focus on the near-nozzle spray behavior for alcohol fuel blends at flashing conditions. The ECN "Spray G" injector, which has been well-characterized previously at non-flashing conditions [14], will be studied here. X-ray radiography, collected at the Advanced Photon Source (APS) at Argonne National Laboratory, will be exploited for fuel density measurements in the near-nozzle region due to the minimal influence of scattering [15] and its ability to generate highly quantitative measurements of fuel mass distribution. Also, specific surface area values will be computed from ultra-small angle X-ray scattering (USAXS) measurements. The results of these two techniques will be combined to yield a Sauter mean diameter (SMD) quantification in the sprays of interest.

Methodology

Experiments were carried out at the 7-BM and 9-ID beamlines of the APS to collect spray radiography and USAXS measurements, respectively [16, 17]. For both techniques, the ECN Spray G #016 injector was mounted in a test vessel fitted with polymide windows for X-ray optical access. The injector was supplied with fuel at 20 MPa

and issued into the chamber which was held at partial vacuum (50 kPa), with a purging flow of nitrogen at 4 and 9.5 standard L·min^{-1} for radiography and USAXS measurements, respectively. The operating conditions are a derivative of the ECN Spray G2, "flash-boiling" conditions, outlined in Table 1 as "G2-cold," since the ambient gas is unheated.

Table 1. Target conditions for radiography and USAXS experiments.

	Spray G2-cold
Fuel	100% iso-octane
Injector temperature, °C	90
Ambient temperature, K	298
Injection pressure, MPa	20
Ambient pressure, kPa	50
Injection command, ms	0.680

Three fuel blends were tested at this flashing condition: iso-octane (i-o), and blends of 80% iso-octane + 20% n-butanol by volume, or 80% iso-octane + 20% ethanol by volume. Properties of single components were sourced from reference tables [18, 19, 20, 21]. Densities of blends were measured, while viscosity and surface tension were calculated based on a linear blending of the components, weighted by the mole fraction of each. These properties of the fuels are provided in Table 2 for reference, where, ρ is the liquid density taken at 20°C, T_b is the boiling temperature, $T_{sat,50}$ is the saturation temperature at 50 kPa, μ_{75} is the viscosity at 75°C, and σ_{50} is the surface tension at 50°C.

Table 2. Properties of tested fuel blends (bold) and their components.

	ρ, kg·m^3	T_b, °C	$T_{sat,50}$, °C	μ_{75}, mPa·s	σ_{50}, mN·m
100% iso-octane	692.7	99.3	76.1	0.289	18.77
100% n-butanol	810.0	117.3	99.0	0.833	22.69
100% ethanol	789.0	78.4	61.5	0.476	19.89
80% i-o, 20% n-butanol	714.5			0.458	19.70
80% i-o, 20% ethanol	710.8			0.366	19.05

Radiography

The diagnostic layout for X-ray radiography measurements collected at the 7-BM beamline are illustrated in Figure 1. The application of the radiography methodology to fuel sprays is thoroughly described in previous works [15, 22]. Specifically here, the synchrotron-produced X-ray light was conditioned to 8.0±0.01 keV mean photon energy (4% ΔE/E) using a double-multilayer monochromator. The incoming beam was sized to a 1.3 × 1.3 mm square cross-section with beam-defining slits and the incident beam intensity, I_0, was measured using a diamond monitor. The beam was then focused using a pair of Kirkpatrick-Baez [23] mirrors to a waist of 4 × 6 µm (V × H) located at the tip of the injector at the experimental origin. After transmission through the spray region of interest, the beam intensity, I, was measured with a PIN diode. This intensity was measured in synchronization with the repetitive injection timing and time averaged over the storage-ring orbit period of 3.68µs, defining the temporal resolution of the measurement. At each spatial location, this time history was recorded and ensemble averaged for 32 injection events to improve the signal-to-noise.

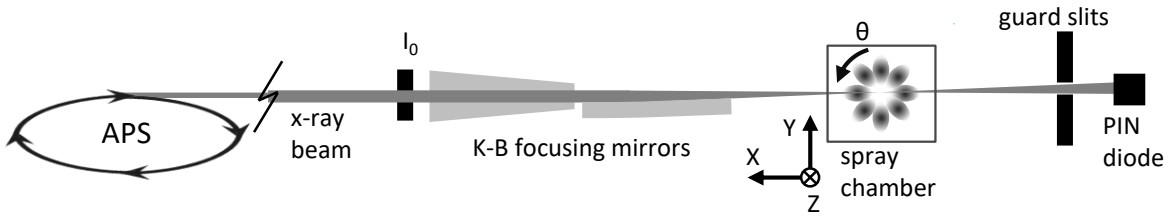

Figure 1. Layout of the radiography experiment.

Following the Beer-Lambert law, the projected mass of the spray (M) within the X-ray path was computed from the beam intensity measurements as described by:

$$M\left(x,y,\theta,t\right)=-\frac{1}{\mu}\log\left[\frac{I\left(x,y,\theta,t\right)}{I_0\left(t\right)}\right], \tag{1}$$

where μ is the mass attenuation coefficient, which was empirically collected. The parameters $I_0\,(t)$ and $I\,(x, y, \theta, t)$ are the measured beam intensities of the incident beam and the transmitted beam, respectively. These measurements were collected for a sequence of locations, transverse to the injector axis, at a fixed distance. Furthermore, transverse scans were collected at a set of rotation angles, θ of the injector to capture projected mass profiles at multiple viewing angles.

Ultra-small-angle X-ray scattering

USAXS measurements were carried out at the 9-ID beamline [17] of the APS, using a Bonse-Hart instrument as schematized in Figure 2. In this configuration, the incoming X-ray light has been conditioned to 21 keV photon energy (λ = 0.59 Å) using a monochromator, and profiled to 50 $\times$ 500 µm (V $\times$ H) with beam-defining slits. The X-rays then interact with a pair of Si (220) crystals arranged as a collimating optic that subjects the light to multiple Bragg reflections, thus resulting in a beam with minimal angular divergence. The beam intensity is then measured with a windowless ion chamber for high accuracy without introduction of parasitic scattering. The beam then passes into the test chamber, and interacts with the pulsed spray, scattering the photons at small angles.

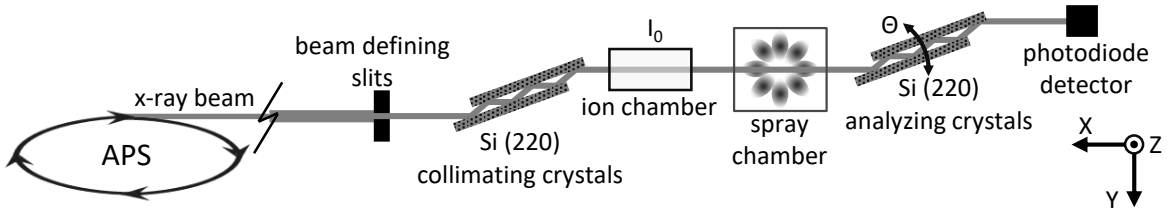

Figure 2. Layout of the USAXS experiment.

During the spray characterization measurements, the injector was commanded for a 1.3 ms injection duration and acquisition was synchronized to occur during 1 ms of the steady-state portion of injection. A total integration time of 40 ms was used for each measurement. Background signal measurements were collected 100 ms prior to injection events to account for the influence of lingering spray in the chamber between events.
The next pair of Si (220) analyzing crystals can precisely rotate to reject light that does not meet the Bragg condition at a range of angles, or scattering vectors, q defined by,

$$q = \frac{4\pi}{\lambda} \sin \Theta, \tag{2}$$

where, λ is the X-ray wavelength, and Θ is half of the angle between the incident and scattered beam. The intensity of this angularly-selected light is then measured with a photodiode. To observe the scattering profile, the intensity was measured for scattering vectors -6.45 $\times$ $10^{-5} \leq$ q $\leq$ 0.050 $Å^{-1}$. The scattering intensity, $I\,(q)$ can be measured and related to the differential cross-section through the following relation [24],

$$I\,(q) = I_0\,\tau\,T\,\epsilon\,\Omega\,\frac{d\Sigma}{d\Omega}\,(q)\,, \tag{3}$$

where, I_0 is the incident X-ray intensity, τ is the sample thickness, T is the sample transmission, ϵ is the efficiency of the detector, Ω is the detector solid angle, and $d\Sigma/d\Omega$ is the differential scattering cross-section per unit volume per unit solid angle. All but the differential cross-section are characterized for the experiment, resulting in a direct comparison of this quantity to the scattering vector, q.
Signal collected for $q <$ 1$\times$ 10^{-4} $Å^{-1}$ was indistinguishable from the background signal, as a result of the angular precision of the instrument, the incident beam divergence, and the bandwidth. Furthermore, for $q >$ 1$\times$ 10^{-2} $Å^{-1}$, weak signal prohibited usable measurements above this range. Of the two limiting cases [25] of correlations between the scattering vector and the differential cross-section, Porod's Law [26], applicable to large q, was exploited for the present study. In this regime, the X-ray wavelength is small compared to the particle size, and the differential scattering cross-section follows a q^{-4} relation, as defined by,

$$\frac{d\Sigma}{d\Omega}\,(q) = 2\pi\,\Delta\rho^2\,S\,q^{-4}, \tag{4}$$

where, S is the surface area per beam area, and $\Delta\rho$ is the scattering length contrast of the particles compared to the surrounding medium,is determined analytically. As applied here, this relationship assumes that the particles are homogeneous, relatively dilute, and locally non-interacting. Furthermore, it is assumed that the particles are randomly oriented which is expected to hold for this gasoline-type spray. Thus, using the Irena software for analyzing the USAXS measurements [27], the spray surface area can be deduced for each probe volume.

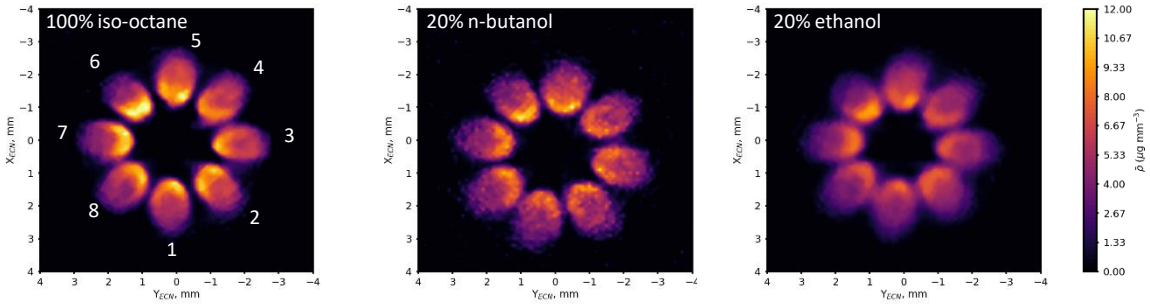

Figure 3. Tomographic reconstructions of X-ray spray radiography, time-averaged between 0.6 and 0.8 ms after command, and plotted in the ECN "Primary" orientation.

Results and discussion

Fuel distribution

The projected mass profiles, collected at individual rotation angles θ, were applied to generating X-ray tomographic radiography, as described in previous studies for characterizing asymmetric sprays [28]. Similarly, a penalized maximum likelihood algorithm was used to reconstruct the ensemble-averaged density fields at each time step [29]. The resulting tomography slices are presented in Figure 3 for the three fuels, time-averaged over the steady portion of the spray (0.6 - 0.8 ms after command). The profiles are depicted in the ECN "Primary" view [12], and the ECN plume numbering is provided in the figure.

These profiles provide a transverse slice of the fuel mass per volume for each condition. Comparing each case, there is consistency in the asymmetry of fuel distribution, where higher peak density values are measured for holes 5 and 6. The distribution of mass for these peak values is more concentrated for the neat iso-octane, potentially indicating a continued breakup and distribution of a more cohesive liquid jet at this downstream location.

Furthermore, the separation between the plumes is more distinct for the neat iso-octane and the blend with n-butanol than in the ethanol blend. This is an indication of a more promoted expansion and therefore plume collapse phenomena as observed at flash-boiling conditions [10].

Referring to Table 2, the property that stands out within these fuel blends is the saturation temperature for the constituents at the 50 kPa condition, with iso-octane ($T_{sat,50}$=76.1 °C) and, more so, the ethanol ($T_{sat,50}$=61.5 °C) being below the 90 °C operating temperature of the injector. Meanwhile, the n-butanol has a saturation temperature above the operating temperature. Since the hot and pressurized condition within the injector would cause the ethanol to be in the greatest superheated state as it emerges from the nozzle, a rapid expansion would take place during injection, which could enhance the jet velocity above that of the other two blends. This hypothesis is also supported by the collapsing plume and homogeneous mass distribution within the plumes visible for the ethanol case in Figure 3.

The differences in spray behavior for each blend can also be quantified by integrating the projected mass (M) at a fixed axial distance, for each time step. This transverse integrated mass (TIM) is derived as,

$$\mathrm{TIM}\,(t) = \int\int \rho_{\mathrm{fuel}}\,(x, y, t)\,dy\,dx, \tag{5}$$

where, ρ_{fuel} is the fuel mass per volume as obtained through the tomographic reconstructions at a given axial slice. This time-resolved, integrated quantity is plotted for each of the blends in Figure 4. Here, the histories for the neat iso-octane and the blend with n-butanol are similar, while the ethanol blend has a consistently lower TIM. It should be noted that the rise in TIM for the Butanol blend occurs approximately 10 μs after the other profiles due to a variation in the triggering methodology. However, the transient nature of the spray and the velocity of the leading plume is not considered in this discussion and analysis.

Considering the same injection pressure and measured valve profiles, the TIM histories should match between the fuel blends and also be conserved as the spray develops downstream (+Z), unless the discharge behavior greatly differs. Considering the proximity to the nozzle, a discrepancy in the TIM would indicate a difference in the supply mass flow rate of liquid, or a change in jet velocity. Since the inflow conditions and the pintle valve motion were consistent between cases, the discharge velocity must differ.

It is observed in diesel sprays, at low ambient density, that the TIM is consistent at different axial distances, most likely due to the minimal amount of entrainment of the ambient gas [15]. In contrast, the GDI design for enhanced entrainment causes a decrease in TIM with axial distance [30], which can be used to compute the relative change in the mass-averaged velocity, v_{ma} between distances [31]. Similarly, for a given axial location and accounting for liquid density differences, this comparison can be made between conditions to characterize the relative average velocity as defined by:

$$\frac{v_{ma}}{v_{ref}} = \frac{\mathrm{TIM}_{ref}/\rho_{ref}}{\mathrm{TIM}/\rho}. \tag{6}$$

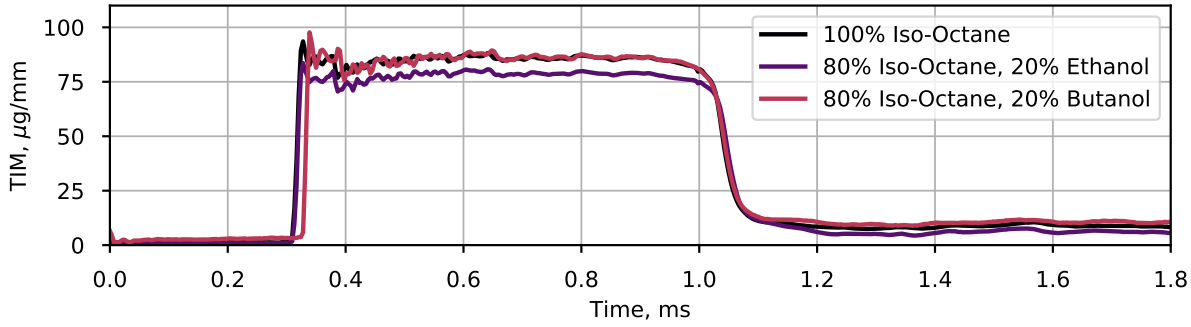

Figure 4. Transverse integrated mass of X-ray spray radiography for each fuel blend at Z = 1 mm.

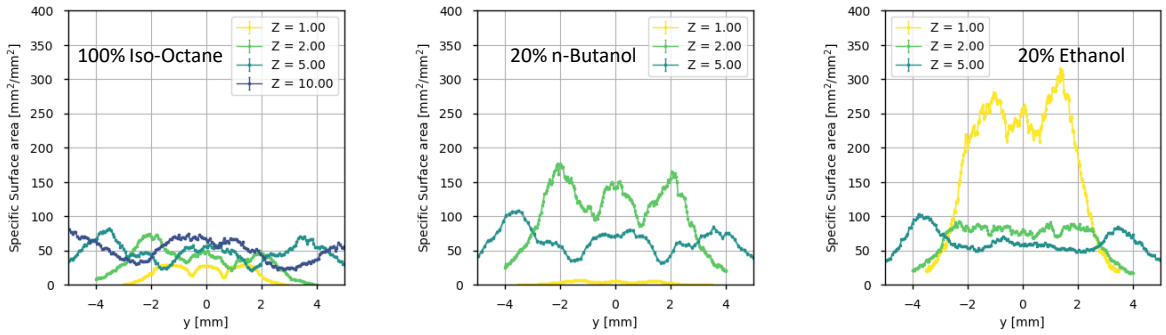

Figure 5. Transverse profiles of the specific surface area for each of the fuel blends at multiple axial distances.

The time-averaged TIM during the steady-state portion of injection for the fuel blends was compared to the neat iso-octane as the reference condition, accommodating for different liquid densities. As illustrated in Figure 4, the n-butanol blend differs only by 1.7% from the iso-octane, whereas, the mass-averaged velocity for the ethanol blend is 11.8% greater.

Specific surface area

To further understand the nature of the sprays and the breakup process, droplet sizing measurements for the same fuels and conditions were collected. Following previous work aimed at simplifying droplet surface area measurements [32, 33], the detailed measurements of complete rocking curves at each spatial location were forgone for a subset within a particular condition.

A detailed USAXS rocking curve was collected at one to three transverse (Y) locations for each axial (Z) distance, while a complete profile of intensities was collected at a fixed q for 200 transverse locations. Profiles were collected and scaled for the three fuel blends at several axial distances from the injector, as illustrated in Figure 5.

Considering that the profiles were scanned in the Y-dimension, the expected projection for this ECN “Primary” view is to resolve three plumes, which can be seen in some of the cases and axial distances. However, the absolute values for specific surface area vary greatly between the different fuels, and as a function of axial distance within a given fuel case. It is noted that the mean value for surface area remains the most consistent for iso-octane as the scans progress in axial distance. Whereas, for the n-butanol blend, the near-nozzle measurements are very low, suggesting that there are likely large, unbroken ligaments of liquid that do not contribute to the scattering signal as much as smaller droplets. Progressing downstream, though, the n-butanol blend has a marked rise in surface area at 2 mm, and then a lower absolute signal at 5 mm, where the spray has also widened. In contrast, the surface area values for the ethanol blend are one to two orders of magnitude higher than the other fuel cases at Z=1 mm. This could be caused by significant disintegration of the liquid into many particles with interfacial boundaries contributing to the scattering signal. At the 2 mm and 5 mm locations, this signal has decreased, suggesting that those droplets have either coalesced or evaporated. It should also be noted that the diagnostic is insensitive to the direction of the density gradient, so small liquid bubbles within a larger ligament can also produce the same specific surface area effect as the same diameter droplet.

Particle sizing

Assuming that there are only spherical particles in our measurement volume, specific surface area measurements can be combined with the measurement of liquid volume in the probe region by X-ray radiography to yield the Sauter

mean diameter (SMD, d_{32}) of the droplets through the following relation:

$$d_{32} = 6\frac{V}{S}, \tag{7}$$

where, S was collected through the USAXS measurements, and V obtained from radiography. This computation was made using transverse USAXS scans taken at Z = 1 mm and the corresponding radiography projections for each fuel condition. These SMD profiles are plotted in Figure 6 on a semi-log scale to highlight the variability between the conditions.

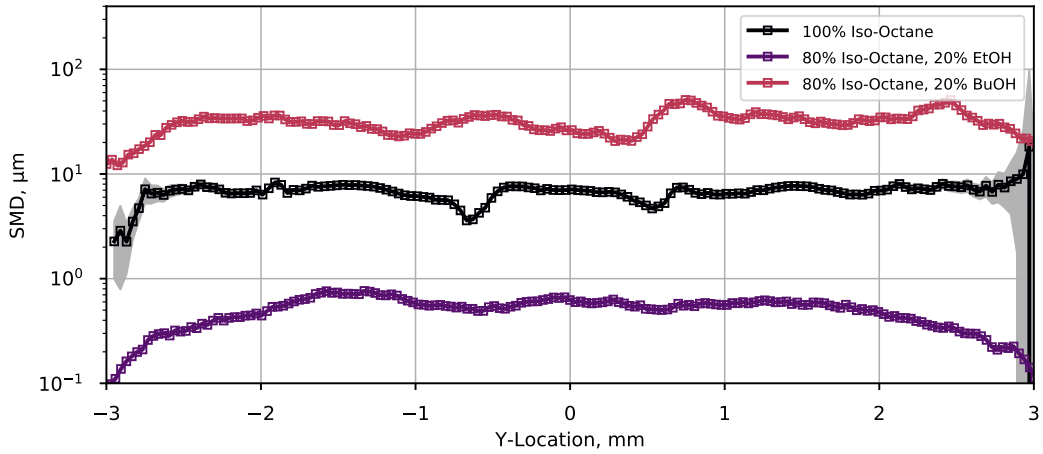

Figure 6. Transverse profiles of SMD for each of the fuels at Z = 1 mm.

When plotted as SMD, the characteristic plume separations are suppressed, which may be caused by the relatively large cross section of the beam, or that the measurements are line-of-sight projections through the spray. The transverse plot of SMD also highlights the differences in the atomization of the different fuel blends. In particular, the diameter of iso-octane droplets at this near-nozzle location appear to be on the order of 10 µm, which agrees with other works at these elevated temperatures and partial-vacuum conditions [34]. Additionally, the observation of larger droplets from the n-butanol blend are supported by the higher viscosity and surface tension, which cause resistance to breakup. The higher saturation temperature for n-butanol is additional contrast to the other two cases, which may limit the effect of flashing in this blend. Conversely in the ethanol blend, the previously-discussed mass distribution and spray surface area, and here, the derived SMD, point to a flash-boiling-promoted discharge and severe fragmentation of the liquid iso-octane. Although spherical particles are assumed for this analysis, which may need to be validated, the trend of droplet sizing is a helpful comparison between the cases.

Summary and Conclusions

This work has investigated the near-nozzle spray behavior for a GDI injector, operating at elevated injection temperatures, into a sub-atmospheric environment. Three fuel blends were tested: neat iso-octane and blends of 80% iso-octane with either 20% n-butanol, or 20% ethanol, by volume.

Quantitative spray radiography measurements were made and processed using computed tomography to deduce the fuel mass per volume mapping in the transverse plane. The density plane for iso-octane showed the most concentrated peak intensities, while the ethanol blend had the most dispersed plumes. Furthermore, the interaction between plumes is more apparent for the ethanol blend at the measured axial distance of 1 mm, indicating that the tendency for spray collapse is greater for this case. The transverse integrated mass histories showed good agreement between the neat iso-octane and n-butanol blend, while the ethanol blend exhibited an 11% greater mass-averaged velocity over the neat iso-octane case.

Additionally, ultra-small-angle X-ray scattering measurements were collected following a recently pioneered efficient methodology. This allowed for the collection of specific surface area profiles across the spray at multiple axial distances. At 1 mm, the n-butanol blend showed a markedly lower surface area than the neat iso-octane, with increased values farther downstream, indicating a progressive atomization. On the other hand, the ethanol blend had much higher surface area at 1 mm, indicating a thoroughly atomized droplet field.

The combined radiography and USAXS measurements were used to compute the Sauter mean diameter profile for the common axial position of 1 mm. The range of values for each fuel condition further illustrates the difference in atomization behavior in reference to neat iso-octane, where the n-butanol blend has larger droplets, which correlate to the higher viscosity, surface tension, and boiling point of the added alcohol. By contrast, the vastly smaller near-nozzle droplets from the ethanol blend with the correlation to much lower boiling temperature of ethanol points to a significantly different atomization process of the liquid.

Although the general topic of flash-boiling sprays has been thoroughly studied, much work is yet to be done on the impact to the atomization mechanism in multi-component fuels. As evidenced here, the properties of different distillates influences the break-up mechanics of the spray. This work serves to provide quantitative metrics for comparison in model development of blended fuel sprays at hot injection and partial vacuum conditions. Through this, improved predictions of atomization characteristics, and thereby combustion performance, can be leveraged in the design for appropriate fuel blending and injector design.

Acknowledgements
This research was conducted as part of the Co-Optimization of Fuels & Engines (Co-Optima) project sponsored by the U.S. Department of Energy (DOE) Office of Energy Efficiency and Renewable Energy (EERE), Bioenergy Technologies and Vehicle Technologies Offices. Research presented in this paper was performed at the 7-BM and 9-ID beamlines at the Advanced Photon Source at Argonne National Laboratory. Use of the APS is supported by the U.S. Department of Energy (DOE) under Contract No. DEAC0206CH11357. Argonne fuel spray research is sponsored by the DOE Vehicle Technologies Program under the direction of Gurpreet Singh and Kevin Stork.

Nomenclature

SMD	=	Sauter mean diameter = d_{32}
TIM	=	Transverse integrated mass
$\Delta\rho$	=	Scattering length contrast compared to the medium
ϵ	=	Detector efficiency
λ	=	Incident light wavelength
μ	=	Mass absorption coefficient
μ_{75}	=	Viscosity at 75°C
Ω	=	Detector solid angle
ρ	=	Liquid density at 20°C
ρ_{fuel}	=	Fuel mass per volume
σ_{50}	=	Surface tension at 50°C
τ	=	Sample thickness
Θ	=	Scattering half-angle
d_{32}	=	Sauter mean diameter
I	=	Measured beam intensity
I_0	=	Reference beam intensity
M	=	Projected mass of the fuel
q	=	USAXS scattering vector
S	=	Total surface area per volume of sample
T	=	Sample transmission
T_b	=	Boiling temperature
$T_{sat,50}$	=	Saturation temperature at 50 kPa
v_{ma}	=	Mass-averaged velocity
v_{ref}	=	Reference velocity

References

[1] F. Zhao, M-C Lai, and D. L. Harrington. *Progress in Energy and Combustion Science*, 25(5):437 – 562, 1999.
[2] H. Zhao. *Advanced Direct Injection Combustion Engine Technologies and Development*, volume 1, chapter 1 - Overview of gasoline direct injection engines, pp. 1 – 19. Woodhead Publishing, 2010.
[3] Georgios Karavalakis, Daniel Short, Diep Vu, Robert L. Russell, Akua Asa-Awuku, Heejung Jung, Kent C. Johnson, and Thomas D. Durbin. *Energy*, 82:168 – 179, 2015.
[4] C. Hergueta, M. Bogarra, A. Tsolakis, K. Essa, and J.M. Herreros. *Fuel*, 208:662 – 672, 2017.
[5] Stefan Heyne and Simon Harvey. *Applied Energy*, 101:203 – 212, 2013. Sustainable Development of Energy, Water and Environment Systems.
[6] Ayhan Demirbas. *Applied Energy*, 86:S108 – S117, 2009. Bio-fuels in Asia.
[7] A. Solomon, S. Rupprecht, L.-D. Chen, and G. Faeth. Atomization and combustion properties of flashing injectors. *20th Aerospace Sciences Meeting*, Aerospace Sciences Meetings. American Institute of Aeronautics and Astronautics, January 1982.
[8] G Zhang, M Xu, T Li, RO Grover, T Kuo, and Y He. *ILASS Americas 26th Annual Conference on Liquid Atomization and Spray Systems*. ILASS Americas, 2014.
[9] Matthew Blessinger, Julien Manin, Scott A Skeen, Maarten Meijer, Scott Parrish, and Lyle M Pickett. *International Journal of Engine Research*, 16(2):238–252, 2015.
[10] Panos Sphicas, Lyle M Pickett, Scott A Skeen, and Jonathan H Frank. *International Journal of Engine Research*, 19(10):1048–1067, 2018.
[11] J. Lacey, F. Poursadegh, M.J. Brear, R. Gordon, P. Petersen, C. Lakey, B. Butcher, and S. Ryan. *Fuel*, 200:345 – 356, 2017.
[12] Sandia National Laboratories. Engine Combustion Network gasoline spray combustion. https://ecn.sandia.gov/gasoline-spray-combustion/, 2019. Accessed March 1, 2019.

[13] E.T. Baldwin, R.O. Grover, S.E. Parrish, D.J. Duke, K.E. Matusik, C.F. Powell, A.L. Kastengren, and D.P. Schmidt. *International Journal of Multiphase Flow*, 87:90 – 101, 2016.
[14] Daniel J. Duke, Alan L. Kastengren, Katarzyna E. Matusik, Andrew B. Swantek, Christopher F. Powell, Raul Payri, Daniel Vaquerizo, Lama Itani, Gilles Bruneaux, Ronald O. Grover, Scott Parrish, Lee Markle, David Schmidt, Julien Manin, Scott A. Skeen, and Lyle M. Pickett. *Experimental Thermal and Fluid Science*, 88(Supplement C):608 – 621, 2017.
[15] Alan Kastengren and Christopher F. Powell. *Experiments in Fluids*, 55(3):1686, Feb 2014.
[16] Alan Kastengren, Christopher F. Powell, Dohn Arms, Eric M. Dufresne, Harold Gibson, and Jin Wang. *Journal of Synchrotron Radiation*, 19(4):654–657, Jul 2012.
[17] Jan Ilavsky, Pete R. Jemian, Andrew J. Allen, Fan Zhang, Lyle E. Levine, and Gabrielle G. Long. *Journal of Applied Crystallography*, 42(3):469–479, Jun 2009.
[18] Robert L. Brown and Stephen E. Stein. *NIST Chemistry WebBook, NIST Standard Reference Database Number 69*, volume 69, chapter Boiling point data. NIST, 2001.
[19] A. A. H. Pádua, J. M. N. A. Fareleira, J. C. G. Calado, and W. A. Wakeham. *Journal of Chemical & Engineering Data*, 41(6):1488–1494, 1996.
[20] David R Lide. *CRC handbook of chemistry and physics*. CRC press, 2005.
[21] E. W. Lemmon, I.H. Bell, M. L. Huber, and M. O. McLinden. NIST Standard Reference Database 23: Reference Fluid Thermodynamic and Transport Properties-REFPROP, Version 10.0, National Institute of Standards and Technology, 2018.
[22] Alan L. Kastengren, F. Zak Tilocco, Daniel Duke, Christopher F. Powell, Xusheng Zhang, and Seoksu Moon. *Atomization and Sprays*, 24(3):251–272, 2014.
[23] Paul Kirkpatrick and A. V. Baez. *J. Opt. Soc. Am.*, 38(9):766–774, Sep 1948.
[24] G. G. Long, P. R. Jemian, J. R. Weertman, D. R. Black, H. E. Burdette, and R. Spal. *Journal of Applied Crystallography*, 24(1):30–37, Feb 1991.
[25] KC Lin, Michael Ryan, Campbell Carter, Alec Sandy, Suresh Narayanan, Jan Ilavsky, and Jin Wang. *ILASS Americas, 21st Annual Conference on Liquid Atomization and Spray Systems*, pp. 18–21, 2008.
[26] Jens Als-Nielsen and Des McMorrow. *Elements of modern X-ray physics*. John Wiley & Sons, 2011.
[27] Jan Ilavsky and Peter R. Jemian. *Journal of Applied Crystallography*, 42(2):347–353, Apr 2009.
[28] Daniel J. Duke, Andrew B. Swantek, Nicolas M. Sovis, F. Zak Tilocco, Christopher F. Powell, Alan L. Kastengren, Doğa Gürsoy, and Tekin Biçer. *SAE International Journal of Engines*, 9(1):143–153, 2016.
[29] Doğa Gürsoy, Francesco De Carlo, Xianghui Xiao, and Chris Jacobsen. *Journal of Synchrotron Radiation*, 21(5):1188–1193, Sep 2014.
[30] Zihan Wang, Andrew Swantek, Riccardo Scarcelli, Daniel Duke, Alan Kastengren, Christopher F. Powell, Sibendu Som, Ronald Reese, Kevin Freeman, and York Zhu. *SAE International Journal of Fuels and Lubricants*, 8(1):147–159, 2015.
[31] Alan L. Kastengren, Christopher F. Powell, Yujie Wang, Kyoung-Su Im, and Jin Wang. *Atomization and Sprays*, 19(11):1031–1044, 2009.
[32] K. E. Matusik, B. A. Sforzo, H. J. Seong, D. J. Duke, A. L. Kastengren, J. Ilavsky, and C. F. Powell. X-ray measurements of fuel spray specific surface area and sauter mean diameter for cavitating and non-cavitating diesel sprays. *ICLASS 2018*. ILASS Americas, 2018.
[33] K. E. Matusik, B. A. Sforzo, H. J. Seong, D. J. Duke, A. L. Kastengren, J. Ilavsky, and C. F. Powell. *Atomization and Sprays*, 2019. Under Review.
[34] P.G. Aleiferis, J. Serras-Pereira, Z. van Romunde, J. Caine, and M. Wirth. *Combustion and Flame*, 157(4):735 – 756, 2010.